# Dynamic contact angle modeling for simulations of drop impingement

**By L. Brown, D. Rossinelli AND P. Moin**

This work presents drop impingement simulations of hexadecane on a flat glass plate. Essential to this work is dynamic contact angle modeling. Building on our previous research employing a modified Cox–Voinov model to drop sliding simulations, we apply this framework to drop impingement. We introduce a numerical method to impose the dynamic contact angle boundary condition that requires no tunable parameters and has improvements to accuracy over other discretizations. Incorporating dynamic contact angles into drop-resolved simulations yields improved agreement with experiments compared to imposing a fixed equilibrium contact angle boundary condition. We consider low capillary and Weber numbers, although the framework presented is general and can be extended to other liquids, surfaces, and contact-angle models.

## 1. Introduction

The angle formed at the intersection of a liquid–gas interface with a solid surface is referred to as a contact angle. Contact angles are ubiquitous in multiphase flows, playing a central role in drop dynamics and, therefore, many everyday processes. The prediction of contact angles has implications for a wide variety of fields, including bioprinting, tissue engineering, pharmaceuticals, smart functional coatings, aerospace engineering, and flexible electronics (Mohammad Karim 2022). As shown in Figure 1, water droplets demonstrate a wide range of contact angles depending on how they interact with the surfaces they touch. The accurate prediction of multiphase flow dynamics often requires the incorporation of contact angle dynamics into drop-resolved simulations.

This study builds on our previous work by applying the contact angle boundary condition developed by Brown & Moin (2024), based on the Cox–Voinov model (Cox 1986; Voinov 1976), to simulations of drop impingement. Furthermore, we present a novel numerical method to impose contact angle boundary conditions into drop-resolved phase-field simulations. This method, unlike many energy functional (Yue 2020) or slip boundary condition methods, limits the number of tunable parameters needed.

The research brief is organized as follows. First, we introduce the governing equations and numerical methodology. Next, we discuss the boundary condition modeling and numerical treatment. Lastly, we present dynamic contact angle simulations of drop impingement and compare the results with experimental data from Yan & Kavehpour (2024).

## 2. Methodology

### 2.1. *Governing Equations*

We use a multiphase, incompressible formulation, with a phase-field treatment of the interface. The interface advection equation used in this work, the accurate conservative

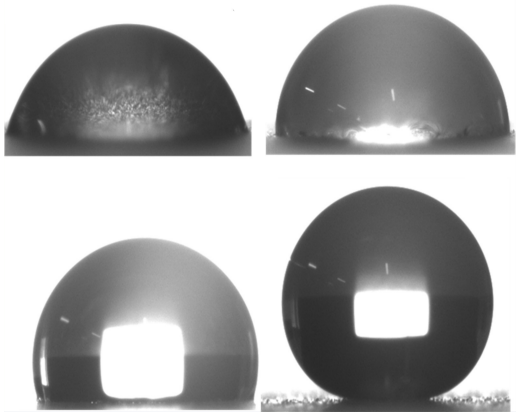

FIGURE 1. A water droplet exhibiting different contact angles when the wall material is varied (Bharathidasan *et al.* 2014).

diffuse interface (ACDI) equation (Jain 2022), is

$$\frac{\partial \phi}{\partial t} + \nabla \cdot (\mathbf{u}\phi) = \nabla \cdot \left[ \Gamma \left[ \epsilon \nabla \phi - \frac{1}{4} \left( 1 - \tanh^2 \left( \frac{\psi}{2\epsilon} \right) \right) \hat{\mathbf{n}} \right] \right] + \phi (\nabla \cdot \mathbf{u}), \tag{2.1}$$

where $\phi$ is the volume fraction, $\mathbf{u}$ is the velocity vector, $\Gamma$ is a stiffness coefficient, $\psi$ is the signed distance function, $\epsilon$ is the interfacial thickness, and $\hat{\mathbf{n}}$ is the interface normal. Equation (2.1) is solved alongside the momentum equations and a variable-coefficient Poisson equation for the pressure. The momentum equation is

$$\frac{\partial \rho \mathbf{u}}{\partial t} + \nabla \cdot (\rho \mathbf{u} \otimes \mathbf{u}) = -\nabla p + \nabla \cdot (\mathbf{f} \otimes \mathbf{u}) + \nabla \cdot \tau + \sigma \kappa \nabla \phi + \rho \mathbf{g}, \tag{2.2}$$

where $\rho$ is the density, $P$ is the pressure, $\mathbf{f}$ is the phase-field mass correction term (Jain 2022), $\boldsymbol{\tau}$ is the viscous stress tensor, $\sigma$ is the surface tension coefficient, and $\mathbf{g}$ is the acceleration due to gravity. The Poisson equation solved is,

$$\nabla \cdot \left( \frac{1}{\rho} \nabla P \right) = \frac{\nabla \cdot \mathbf{u}^*}{\Delta t}, \tag{2.3}$$

where $\mathbf{u}^*$ is the intermediate velocity field of the fractional step method (Kim & Moin 1985) and $\Delta t$ is the timestep. All simulations use periodic boundary conditions in the wall-parallel directions, a no-slip wall at the bottom of the domain, and a slip wall at the top. A no-penetration boundary condition is also used at the top and bottom walls for the wall-normal velocity field and the mass fluxes in Eq. (2.1).

### 2.2. *Numerical treatment*

The code used herein is a multiphase flow solver that is staggered grid, fourth order explicit in time (with the exception of the surface tension term, which is treated implicitly), and second order central in space. Time advancement is performed with a four-stage, fourth-order explicit Runge–Kutta scheme. Equations (2.1), (2.2), and (2.3) are discretized and solved in turn during each RK substep. The pressure Poisson equation in Eq. (2.3) is solved using a transform method and a technique that is similar to as done in Dodd & Ferrante (2014). More details about code performance are presented in

Rossinelli *et al.* (2025). We use

$$\epsilon = \max(\Delta x, \Delta y, \Delta z) \tag{2.4}$$

as the characteristic interface thickness.

The timestep $\Delta t$ and the interface regularization stiffness parameter $\Gamma$ are both chosen such that the interface regularization terms in Eq. (2.1) are the stiffest terms in the system of equations, in the sense that they have the most restrictive timestep requirement. For this process, a precursor $\Delta t_{\text{stiff}}$ is first chosen based on the minimum of the convective and viscous timestep restrictions,

$$\Delta t_{\text{stiff}} = \min\left(\frac{\Delta s}{|\mathbf{u}|_{\max}}, \frac{\rho_l(\Delta s)^2}{6\mu_l}, \frac{\rho_s(\Delta s)^2}{6\mu_s}\right), \tag{2.5}$$

where the $l$ and $s$ subscripts denote the liquid and gas phases in the domain respectively. Here, $\Delta s = \min(\Delta x, \Delta y, \Delta z)$. We now specify that the timestep restriction for ACDI is more restrictive than for the other terms,

$$\Delta t_{\text{ACDI}} = C_1 \Delta t_{\text{stiff}}, \tag{2.6}$$

for some $C_1 \leq 1$. Since the stability requirements for ACDI (Jain 2022) require

$$\Delta t_{\text{ACDI}} = \frac{(\Delta s)^2}{6\Gamma\epsilon}, \tag{2.7}$$

then solving for $\Gamma$ we have

$$\Gamma = \frac{(\Delta s)^2}{6C_1\epsilon\Delta t_{\text{stiff}}}. \tag{2.8}$$

Additionally, in the limit that advection, $\Delta t_{adv} = \Delta s/|\mathbf{u}|_{\max}$, is the most limiting timestep restriction, then the stability requirements of ACDI require $\Gamma = |\mathbf{u}|_{\max}$ (Jain 2022). Hence, $C_1 = \Delta s/(6\epsilon)$. This makes the ACDI timestep

$$\Delta t_{\text{ACDI}} = \frac{\Delta t_{\text{stiff}}}{6}, \tag{2.9}$$

and the interface regularization stiffness coefficient

$$\Gamma = \frac{\Delta s}{\Delta t_{\text{stiff}}}. \tag{2.10}$$

Finally, the overall simulation timestep is set as $\Delta t = C_2 \Delta t_{\text{ACDI}}$ where $C_2$ is an adjustable stability parameter.

## 3. Contact angle boundary condition

### 3.1. *Dynamic contact angle modeling*

The dynamic contact angle boundary condition used in this work is an improved version of the dynamic Cox–Voinov model (Cox 1986; Voinov 1976), described by Brown & Moin (2024) as

$$\theta = \theta_d = \left(\theta_s^3 + 9\frac{\mu_l(\mathbf{U}\cdot\hat{\mathbf{n}}')}{\sigma}\ln\left(\frac{l_{\text{cap}}}{l_{\text{slip}}}\right)\right)^{1/3}, \text{ where } \quad \hat{\mathbf{n}}' = \frac{\left[\frac{\partial\psi}{\partial x} \quad 0 \quad \frac{\partial\psi}{\partial z}\right]}{\sqrt{(\frac{\partial\psi}{\partial x})^2 + (\frac{\partial\psi}{\partial z})^2}}. \tag{3.1}$$

Here, $\theta_s$ is the static contact angle, $\mu_l$ is the dynamic viscosity of the liquid, $\mathbf{U}$ is a directional characteristic velocity, $\sigma$ is the surface tension, $l_{\text{cap}}$ is the capillary length

scale, $l_{\text{slip}}$ is the molecular slip length, and $\hat{\mathbf{n}}'$ is the unit vector that is both normal to the drop footprint on the wall and tangent to the wall surface. The model presented in Eq. (3.1) takes into account the directionality of the velocity field through the dot product $\mathbf{U} \cdot \hat{\mathbf{n}}'$, as described by Brown & Moin (2024). The boundary condition is solved at each location along the wall, allowing the dynamic contact angle to vary as a function of space. Thus, at each $(i, k)$ location along the wall, we calculate

$$\theta^{(i,k)} = \left( \theta_s^3 + 9 \frac{\mu_l (\mathbf{U}^{(i,k)} \cdot \hat{\mathbf{n}}'^{(\mathbf{i},\mathbf{k})})}{\sigma} \ln \left( \frac{l_{\text{cap}}}{l_{\text{slip}}} \right) \right)^{1/3}, \tag{3.2}$$

where

$$\hat{\mathbf{n}}'^{(i,k)} = \frac{\left[ \frac{\partial \psi}{\partial x}|_{(i,k)} \quad 0 \quad \frac{\partial \psi}{\partial z}|_{(i,k)} \right]}{\sqrt{(\frac{\partial \psi}{\partial x}|_{(i,k)})^2 + (\frac{\partial \psi}{\partial z}|_{(i,k)})^2}}. \tag{3.3}$$

The dynamic contact angles calculated in Eq. (3.2) are imposed into the simulation through a layer of scalar ghost values of $\psi$ below the wall location. In setting the ghost values of $\psi$, this also fully determines the ghost values of $\phi$, $\rho$, and $\mu$, since there is a closed-form algebraic relationship between the signed distance function $\psi$ and these quantities. Additionally, ghost values for the interface normal vector, $\hat{\mathbf{n}}$, must be imposed. These ghost values together couple into the simulation primarily through affecting the surface tension term of the momentum equation near the wall. Thus, the dynamic contact angle imposed influences the forces felt by the drop at the wall, which in turn affects drop dynamics.

### 3.2. *Numerical treatment of ghost points*

To impose the dynamic contact angle into the simulation by populating ghost points of $\psi$, the geometric relation from Ding & Spelt (2007) is used,

$$\tan \left( \frac{\pi}{2} - \theta \right) = \frac{n_y}{n_\tau}. \tag{3.4}$$

Here, $n_y$ is the wall-normal component of the interface normal and $n_\tau$ is the wall-parallel component of the interface normal at the wall. Equation (3.4) is illustrated geometrically in Figure 2. Now, Eq. (3.4) must be discretized. The near-wall grid setup of the domain is shown in Figure 3. In Griebel & Klitz (2013), $n_y$ is discretized using central differences about the wall. However, $n_\tau$ is discretized about the $j = 0$ location, which introduces an $O(\Delta y)$ error in the discretization. In this work, the $n_y$ and $n_\tau$ derivatives are both discretized using second-order central finite difference directly at the wall location, $j = -1/2$. As a consequence, the resulting discrete equation is nonlinear in the ghost points, $\psi^{(i,-1,k)}$. Much of the remainder of this subsection is devoted to formulating and solving this nonlinear system of equations.

Noting that $\hat{n} = \nabla\psi / |\nabla\psi|$, we can discretize and manipulate Eq. (3.4) to obtain,

$$\left. \frac{\partial \psi}{\partial y} \right|_{\text{wall}}^{(i,k)} = \left| \frac{\partial \psi}{\partial \tau} \right| \Bigg|_{\text{wall}}^{(i,k)} \tan \left( \frac{\pi}{2} - \theta^{(i,k)} \right). \tag{3.5}$$

Here, $\theta^{(i,k)}$ is an input to the boundary condition, which can be defined using either a static value or the output of a dynamic contact angle such as the one in Eq. (3.2). Next, we define the following helpful quantities. $a^{(i,k)(t_{n+1})}$, which is the derivative of the signed

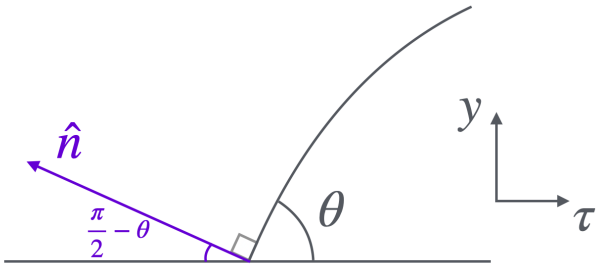


FIGURE 2. Geometric diagram illustrating Eq. (3.4). The $\tau$ axis represents the net direction of the components of the interface normal that are parallel to the wall.

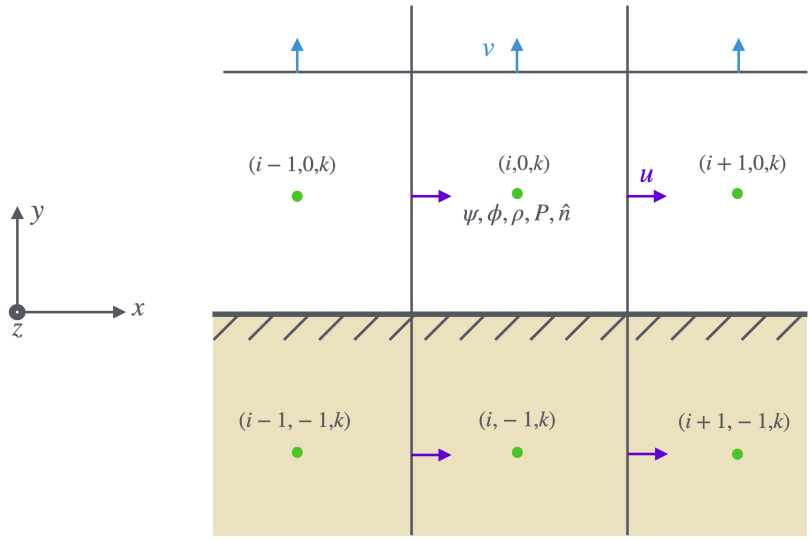


FIGURE 3. The staggered-grid setup used in the code, demonstrated in a two-dimensional plane. The wall is positioned at the index $j = -1/2$. Ghost points are denoted with $j = -1$.

distance function at timestep $t_{n+1}$ in the $x$ direction at the wall, is discretized as

$$\begin{aligned} a^{(i,k)(t_{n+1})} &= \left.\frac{\partial \psi}{\partial x}\right|_{\text{wall}}^{(i,k)(t_{n+1})} \\ &\approx \frac{\psi^{(i+1,0,k)(t_{n+1})} - \psi^{(i-1,0,k)(t_{n+1})} + \psi^{(i+1,-1,k)(t_{n+1})} - \psi^{(i-1,-1,k)(t_{n+1})}}{4\Delta x} \\ &= \Phi_x^{(i,k)(t_{n+1})} + \frac{\Delta\psi^{(i+1,-1,k)} - \Delta\psi^{(i-1,-1,k)}}{4\Delta x}, \end{aligned} \tag{3.6}$$

where

$$\Phi_x^{(i,k)(t_{n+1})} = \frac{\psi^{(i+1,0,k)(t_{n+1})} - \psi^{(i-1,0,k)(t_{n+1})} + \psi^{(i+1,-1,k)(t_n)} - \psi^{(i-1,-1,k)(t_n)}}{4\Delta x}. \tag{3.7}$$

Because Eq. (2.1) is advanced inside the domain before the boundary condition is set, the values of $\psi$ at $j = 0$ and time $t_{n+1}$ are known, whereas the unknown values $\psi^{(i,-1,k)(t_{n+1})}$ are expressed as $\psi^{(i,-1,k)(t_{n+1})} = \psi^{(i,-1,k)(t_n)} + \Delta\psi^{(i,-1,k)}$, where the delta term is as-

sumed to be small. Likewise, we define

$$b^{(i,k)(t_{n+1})} = \left.\frac{\partial \psi}{\partial z}\right|_{\text{wall}}^{(i,k)(t_{n+1})}$$
$$\approx \frac{\psi^{(i,0,k+1)(t_{n+1})} - \psi^{(i,0,k-1)(t_{n+1})} + \psi^{(i,-1,k+1)(t_{n+1})} - \psi^{(i,-1,k-1)(t_{n+1})}}{4\Delta z}$$
$$= \Phi_z^{(i,k)(t_{n+1})} + \frac{\Delta\psi^{(i,-1,k+1)} - \Delta\psi^{(i,-1,k-1)}}{4\Delta z}, \quad (3.8)$$

where

$$\Phi_z^{(i,k)(t_{n+1})} = \frac{\psi^{(i,0,k+1)(t_{n+1})} - \psi^{(i,0,k-1)(t_{n+1})} + \psi^{(i,-1,k+1)(t_n)} - \psi^{(i,-1,k-1)(t_n)}}{4\Delta z}. \quad (3.9)$$

Lastly,

$$c^{(i,k)(t_{n+1})} = \left|\frac{\partial \psi}{\partial \tau}\right|\Big|_{\text{wall}}^{(i,k)(t_{n+1})} \simeq \sqrt{(a^{(i,k)(t_{n+1})})^2 + (b^{(i,k)(t_{n+1})})^2}, \quad (3.10)$$

and

$$\left.\frac{\partial \psi}{\partial y}\right|_{\text{wall}}^{(i,k)(t_{n+1})} \simeq \frac{\psi^{(i,0,k)(t_{n+1})} - \psi^{(i,-1,k)(t_{n+1})}}{\Delta y}. \quad (3.11)$$

Now the goal is to combine Eqs. (3.10) and (3.11) into Eq. (3.5) to construct a linear system with the ghost $\Delta\psi$ values as unknowns. The squares of $a$ and $b$ are linearized as

$$(a^{(i,k)})^2 \simeq (\Phi_x^{(i,k)})^2 + \frac{\Phi_x^{(i,k)}(\Delta\psi^{(i+1,-1,k)} - \Delta\psi^{(i-1,-1,k)})}{2\Delta x}, \quad (3.12)$$

$$(b^{(i,k)})^2 \simeq (\Phi_z^{(i,k)})^2 + \frac{\Phi_z^{(i,k)}(\Delta\psi^{(i,-1,k+1)} - \Delta\psi^{(i,-1,k-1)})}{2\Delta z}. \quad (3.13)$$

Using the Taylor approximation $\sqrt{C+x} \approx \sqrt{C} + x/(2\sqrt{C})$ for small $x$, we obtain

$$c^{(i,k)} \approx S^{(i,k)} + \frac{1}{4S^{(i,k)}}\left(\frac{\Phi_x^{(i,k)}}{\Delta x}(\Delta\psi^{(i+1,-1,k)} - \Delta\psi^{(i-1,-1,k)})\right)$$
$$+ \frac{1}{4S^{(i,k)}}\left(\frac{\Phi_z^{(i,k)}}{\Delta z}(\Delta\psi^{(i,-1,k+1)} - \Delta\psi^{(i,-1,k-1)})\right), \quad (3.14)$$

where $S^{(i,k)} = \sqrt{\left(\Phi_x^{(i,k)}\right)^2 + \left(\Phi_z^{(i,k)}\right)^2}$. Substituting these pieces into Eq. (3.5) yields

$$\Delta\psi^{(i,-1,k)} = \psi^{(i,0,k)(t_{n+1})} - \psi^{(i,-1,k)(t_n)} - (\Delta y)\tan\left(\frac{\pi}{2} - \theta^{(i,k)}\right) S^{(i,k)}$$
$$- (\Delta y)\tan\left(\frac{\pi}{2} - \theta^{(i,k)}\right)\left(\frac{\Phi_x^{(i,k)}}{\Delta x}\frac{\Delta\psi^{(i+1,-1,k)} - \Delta\psi^{(i-1,-1,k)}}{4S^{(i,k)}}\right)$$
$$- (\Delta y)\tan\left(\frac{\pi}{2} - \theta^{(i,k)}\right)\left(\frac{\Phi_z^{(i,k)}}{\Delta z}\frac{\Delta\psi^{(i,-1,k+1)} - \Delta\psi^{(i,-1,k-1)}}{4S^{(i,k)}}\right). \quad (3.15)$$

Equation (3.15) forms a linear system for the unknowns $\Delta\psi^{(i,-1,k)}$ and is obtained by linearizing the nonlinear geometric condition of Eq. (3.5) with respect to the ghost values

$\psi^{(i,-1,k)}$. In practice, this equation is treated within an outer fixed-point iteration on the ghost values. Given a current guess for $\psi^{(i,-1,k)}$, we compute $\Phi_x^{(i,k)}$, $\Phi_z^{(i,k)}$, and $S^{(i,k)}$, assemble the linear system (3.15) for the corresponding $\Delta\psi^{(i,-1,k)}$, and solve Eq. (3.15) in a matrix-free manner using point Jacobi iterations. The ghost values are then updated via

$$\psi^{(i,-1,k)} \leftarrow \psi^{(i,-1,k)} + \Delta\psi^{(i,-1,k)}, \tag{3.16}$$

and the process is repeated until convergence. For notational simplicity, outer-iteration indices on $\psi$, $\Phi_x$, $\Phi_z$, and $S$ have been omitted in Eqs. 3.6–3.15. Additionally, these equations are written with respect to the previous time-step solution $\psi^{(i,-1,k)(t_n)}$, which serves as the initial guess for the outer iteration. However, after the first outer iteration, all quantities, including the initial ghost-point values $\psi^{(i,-1,k)(t_n)}$, are understood to be replaced with the current iterate of the outer loop.

We can prove that the Jacobi iterations for the linearized system of Equation (3.15) converge through the Gershgorin theorem. For the system to have a unique solution, it is sufficient that all of the eigenvalues of $A$, where $A\Delta\psi = b$, be strictly positive. Since the diagonals of $A$ are all unity, the criterion that must be satisfied is

$$R^{(i,k)} = (\Delta y)\left|\tan\left(\frac{\pi}{2} - \theta^{(i,k)}\right)\right| \left(\frac{1}{2\sqrt{\left(\Phi_x^{(i,k)}\right)^2 + \left(\Phi_z^{(i,k)}\right)^2}}\right) \left(\frac{|\Phi_x^{(i,k)}|}{\Delta x} + \frac{|\Phi_z^{(i,k)}|}{\Delta z}\right) < 1. \tag{3.17}$$

In other words, the radius $R^{(i,k)}$ of each Gershgorin disc must be less than unity. Additionally, if Eq. (3.17) holds, then the convergence criterion for the point Jacobi method is also satisfied. This is because Eq. (3.17) guarantees that the matrix $A$ is strictly diagonally dominant. Through the Cauchy–Schwarz inequality, we can prove that, for any $\Phi_x$ and $\Phi_z$,

$$R^{(i,k)} < (\Delta y)\left|\tan\left(\frac{\pi}{2} - \theta^{(i,k)}\right)\right| \left(\frac{1}{2}\right) \sqrt{\frac{1}{(\Delta x)^2} + \frac{1}{(\Delta z)^2}}. \tag{3.18}$$

Therefore, if

$$\Delta y < \frac{2\Delta x \Delta z}{\max_{i,j}\left|\tan\left(\frac{\pi}{2} - \theta^{(i,k)}\right)\right| \sqrt{(\Delta x)^2 + (\Delta z)^2}}, \tag{3.19}$$

then the linear system is guaranteed to converge. In practice, the convergence criteria places a resolution requirement on the wall-normal direction with respect to the wall-parallel resolution. The resolution requirement becomes more stringent the closer the contact angles get to 180° or 0°. For the angles of interest (roughly in the range of 20° to 160°), the additional resolution requirement is not far from what is already required owing to the physics of the problem. Furthermore, one must know beforehand the range of dynamic contact angles to be observed in a simulation in order to properly set the $y$ resolution. For the purposes of this study, the minimum contact angle estimate is set at 30°, which is below the 33° minimum observed experimentally (Yan & Kavehpour 2024).

Solving the aforementioned linear system determines the ghost values of $\psi$. This also fully determines the ghost values of $\phi$, $\rho$, and $\mu$ through the algebraic relationship between $\psi$ and $\phi$, $\rho$, and $\mu$ described in Jain (2022). Finally, the ghost values of the interface

normal, $\hat{\mathbf{n}}$, must be determined. This amounts to calculating

$$\left.\frac{\partial\psi}{\partial y}\right|^{(i,-1,k)}, \quad \left.\frac{\partial\psi}{\partial x}\right|^{(i,-1,k)}, \quad \text{and} \quad \left.\frac{\partial\psi}{\partial z}\right|^{(i,-1,k)}, \tag{3.20}$$

at each $(i,k)$ ghost-point location, and then subsequently normalizing the results into a unit vector, $\hat{\mathbf{n}}$. The wall-parallel derivatives in $x$ and $z$ are straightforward to calculate,

$$\left.\frac{\partial\psi}{\partial x}\right|^{(i,-1,k)(t_{n+1})} \approx \frac{\psi^{(i+1,-1,k)(t_{n+1})} - \psi^{(i-1,-1,k)(t_{n+1})}}{2\Delta x}, \tag{3.21}$$

$$\left.\frac{\partial\psi}{\partial z}\right|^{(i,-1,k)(t_{n+1})} \approx \frac{\psi^{(i,-1,k+1)(t_{n+1})} - \psi^{(i,-1,k-1)(t_{n+1})}}{2\Delta z}. \tag{3.22}$$

On the other hand, the wall-normal derivative is set through an extrapolation using the geometric relation given in Eq. (3.5) and the wall-normal derivative about $j = 0$,

$$\left.\frac{\partial\psi}{\partial y}\right|^{(i,-1,k)(t_{n+1})} \approx 2\left.\frac{\partial\psi}{\partial y}\right|_{\text{wall}}^{(i,k)(t_{n+1})} - \frac{\psi^{(i,1,k)(t_{n+1})} - \psi^{(i,-1,k)(t_{n+1})}}{2\Delta y}. \tag{3.23}$$

Here, $\partial\psi/\partial y|_{\text{wall}}^{(i,k)(t_{n+1})}$ is obtained using Eqs. (3.5) and (3.10) using the converged ghost values of $\psi$. The unit normal $\hat{\mathbf{n}}$ in the ghost points may now be formed as

$$\hat{\mathbf{n}}^{(i,-1,k)(t_{n+1})} = \left(\frac{\nabla\psi}{|\nabla\psi|}\right)^{(i,-1,k)(t_{n+1})}, \tag{3.24}$$

using the quantities from Eqs. (3.21)-(3.23).

## 4. Results

To investigate the performance of the numerical method combined with the dynamic contact angle model, we simulated the $We = 32.4$ case from Yan & Kavehpour (2024). More details about these experiments are given in McGuan *et al.* (2024). A coarse and medium grid were used, and both grids were run once with a static contact angle imposed and once with the dynamic contact angle model fully coupled into the solver. Table 1 lists the physical parameters used in the simulations.

The proper initial drop height needed to match the target Weber number was estimated through the kinematics equations. Since the Weber number is defined as

$$We = \frac{\rho_l v_f^2 D}{\sigma}, \tag{4.1}$$

where $D$ is the drop diameter and $v_f$ is the final velocity magnitude before the drop hits the wall, this can be solved for $v_f$ to yield

$$v_f = \sqrt{\frac{\sigma(We)}{\rho D}}. \tag{4.2}$$

Additionally, the kinematics equations can be used to estimate $v_f$ as a function of drop initial height. Since

$$v_f = |g| t_{\text{impact}} \quad \text{and} \quad h = \frac{1}{2}|g| t_{\text{impact}}^2, \tag{4.3}$$

| Parameter | Value | Description |
|---|---|---|
| Coarse grid ($N_x \times N_y \times N_z$) | ($72 \times 220 \times 72$) | Grid size for the coarse-refinement simulations |
| Medium grid ($N_x \times N_y \times N_z$) | ($100 \times 310 \times 100$) | Grid size for the medium-refinement simulations |
| $Lx$ | 1.25 cm | Domain size in $x$ |
| $Ly$ | 3.1 cm | Domain size in $y$ |
| $Lz$ | 1.25 cm | Domain size in $z$ |
| $\rho_{\text{air}}$ | 1.225 kg/m$^3$ | Density of air |
| $\rho_{\text{hex}}$ | 773 kg/m$^3$ | Density of hexadecane |
| $\mu_g$ | 0.01 kg/(m·s) | Dynamic viscosity of air |
| $\mu_l$ | 5.6 kg/(m·s) | Dynamic viscosity of hexadecane |
| $\sigma$ | 0.02923 kg/s$^2$ | Surface tension coefficient between hexadecane and air |
| $g$ | $-9.81$ m/s$^2$ | Gravity |
| $R_d$ | 1.05 mm | Drop diameter |
| $h_d$ | 2.97 cm | Drop initial height |
| $\theta_s$ | 32° | Static contact angle of hexadecane-glass plate-air |
| $l_{\text{slip}}$ | 20 nm | Molecular slip length of hexadecane on a glass plate |

TABLE 1. The parameters used in the drop impingement simulations. The molecular slip length is estimated from experiments performed in Le Grand *et al.* (2005), where hexadecane is also used.

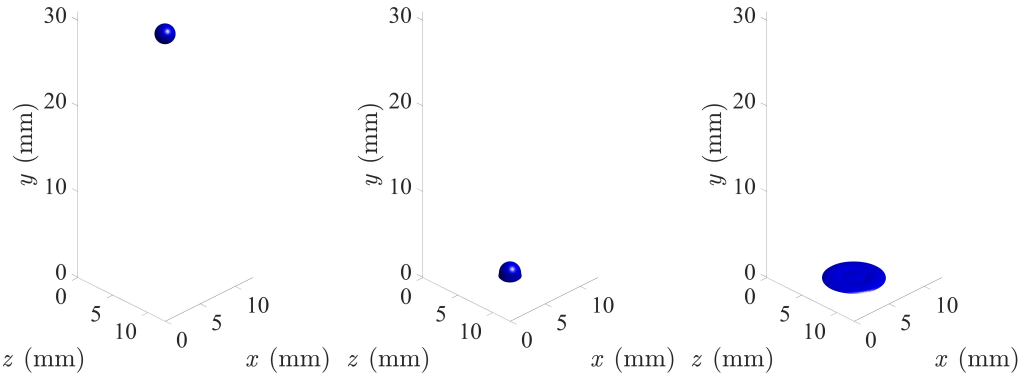


FIGURE 4. Snapshots of the medium-refinement drop impingement simulation with dynamic contact angle modeling enabled. The panels show the $\phi = 0.5$ isocontour of the droplets. (a) The initial condition at $t = -0.0751$ seconds, with the drop beginning at rest. (b) The drop at $t = 4.15 \times 10^{-4}$ seconds as it first collides at the wall. (c) The drop at $t = 0.00750$ seconds spreading upon impact. Here, $t = 0$ is approximately when the drop first touches the plate.

where $t_{\text{impact}}$ is the time between initialization and impact, we have

$$v_f = \sqrt{2|g|h}. \tag{4.4}$$

Combining Eqs. (4.3) and (4.4), we have

$$h = \frac{\sigma(We)}{2\rho D|g|}. \tag{4.5}$$

This provides an estimate of the required drop initial height to achieve a given Weber number.

Furthermore, the velocity at the first grid point above the wall is used as the character-

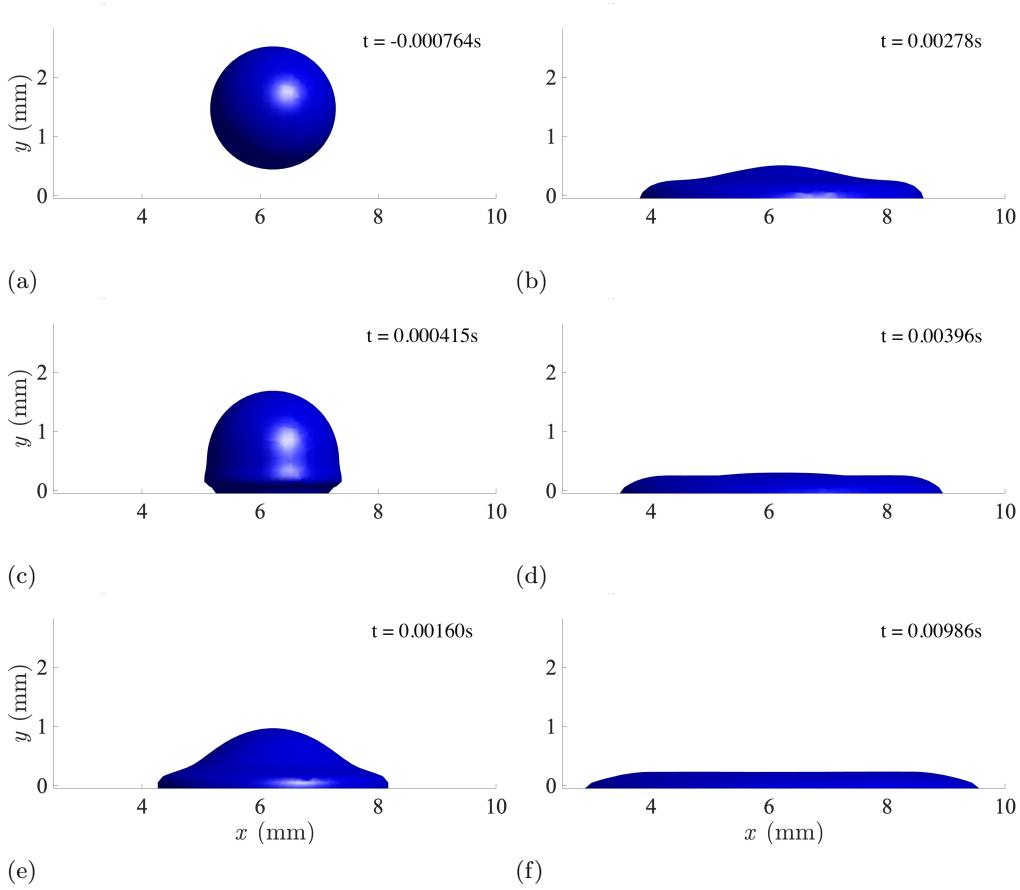


FIGURE 5. Close-up snapshots showing the time evolution of the medium-refinement drop impingement simulation with dynamic contact angle modeling. The panels show the $\phi = 0.5$ isocontour of the droplets, including the ghost value layer of $\phi$ located below $y = 0$. In snapshots (c) and (e), the dynamic contact angle is much greater than the equilibrium contact angle because of the large outward radial velocity. In snapshots (b), (d), and (f), the contact angle decreases towards the equilibrium contact angle as the drop radial velocity reduces. $t = 0$ is approximately when the drop first touches the plate.

istic velocity at each wall location in Eq. (3.2). Snapshots of the medium grid simulation using the dynamic contact angle model from Equation 3.1 are shown in Figures 4 and 5. Figure 5 clearly showcases that the dynamic contact angle model is activated and a dynamic contact angle value is being successfully imposed in the simulation through use of the numerical method described in Section 3. As shown in Figure 6, the use of the dynamic contact angle model yields an improvement in prediction of the drop footprint as a function of time. Additionally, as shown in Figure 7, the dynamic contact angle predicted by the model closely matches the measured experimental results. Future work includes further establishing the grid independence of the computed results and performing simulations of higher Weber number cases.

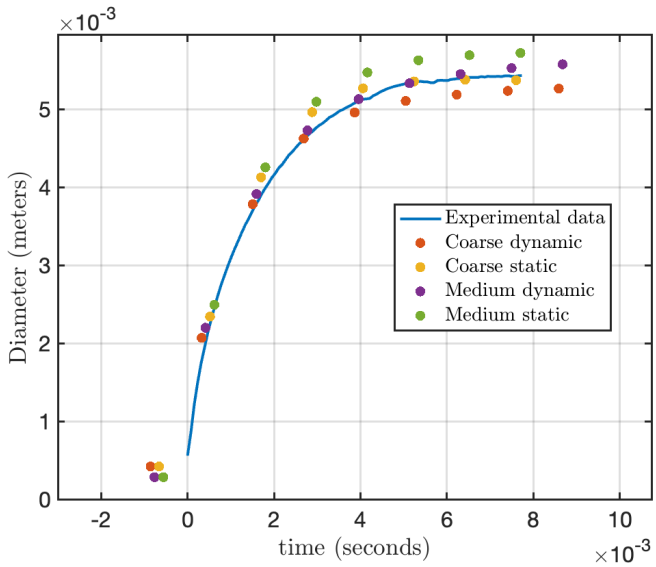


FIGURE 6. Drop footprint versus time for the experiment by Yan & Kavehpour (2024), the coarse- and medium-grid dynamic contact angle simulations, and the coarse- and medium-grid static contact angle simulations. Results are obtained using the parameters in Table 1. Each dataset is aligned such that $t = 0$ corresponds to when the drop approximately first hits the wall. Nonzero diameter values before $t = 0$ are observed for the four simulations as a result of the diffuse nature of the interface.

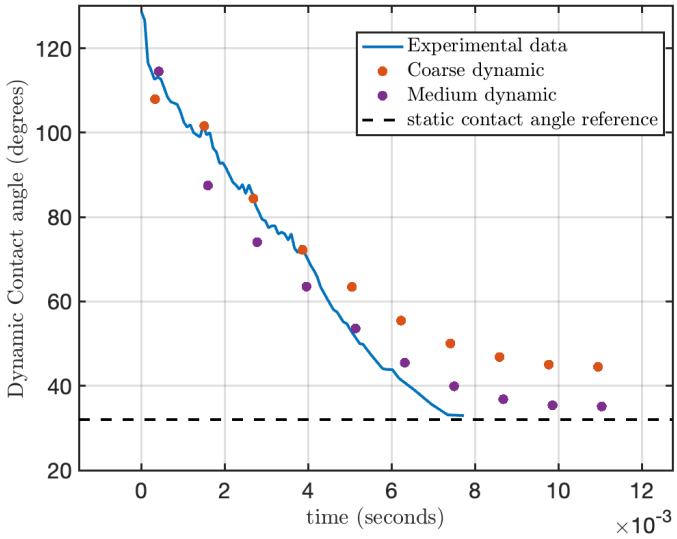


FIGURE 7. Contact angle versus time for the experiment by Yan & Kavehpour (2024), and the coarse- and medium-grid dynamic contact angle simulations. Although the dynamic contact angle is determined on-the-fly during the simulations by Eq. 3.2, the contact angle data plotted here for the simulations is postprocessed by calculating the average contact angle of the drop over the entire drop shape. Results are obtained using the parameters in Table 1.

## 5. Conclusions

This brief presents a numerical method for imposing dynamic contact angles in diffuse-interface simulations of drop impingement. This approach entails setting ghost points of phase-field related quantities through finite-difference approximations, fixed-point iterations, and the point-Jacobi method. We use this method in addition to a directionally-aware dynamic contact angle model from Brown & Moin (2024) to perform simulations of hexadecane droplets impacting a flat glass plate. The resulting simulations show good agreement with the measured spreading and dynamic contact angle measurements from Yan & Kavehpour (2024). We demonstrate improvement when the dynamic contact-angle model is enabled over when a solely static contact angle is imposed. The presented results highlight the importance of dynamic contact angle modeling. The framework presented here is general and can be extended to other liquids, surfaces, and contact-angle models.

*Acknowledgments*

This work is supported by the US Department of Energy, Office of Science, Office of Advanced Scientific Computing Research; a Department of Energy Computational Science Graduate Fellowship (award DE-SC0023112); Boeing; and NASA. We thank Federico Zabaleta for his insightful comments and Yan & Kavehpour (2024) for providing experimental data.

## REFERENCES

Bharathidasan, T., Kumar, S. V., Bobji, M., Chakradhar, R. & Basu, B. J. 2014 Effect of wettability and surface roughness on ice-adhesion strength of hydrophilic, hydrophobic and superhydrophobic surfaces. *Appl. Surf. Sci.* **314**, 241–250.

Brown, L. & Moin, P. 2024 Diffuse interface boundary conditions for dynamic contact angles. *Annual Research Briefs,* Center for Turbulence Research, Stanford University, pp. 281–291.

Cox, R. G. 1986 The dynamics of the spreading of liquids on a solid surface. Part 1. Viscous flow. *J. Fluid Mech.* **168**, 169–194.

Ding, H. & Spelt, P. D. M. 2007 Wetting condition in diffuse interface simulations of contact line motion. *Phys. Rev. E* **75**, 046708.

Dodd, M. S. & Ferrante, A. 2014 A fast pressure-correction method for incompressible two-fluid flows. *J. Comput. Phys.* **273**, 416–434.

Griebel, M. & Klitz, M. 2013 Simulation of droplet impact with dynamic contact angle boundary conditions. In *Singular Phenomena and Scaling in Mathematical Models*, pp. 297–325. Springer.

Jain, S. S. 2022 Accurate conservative phase-field method for simulation of two-phase flows. *J. Comput. Phys.* **469**, 111529.

Kim, J. & Moin, P. 1985 Application of a fractional-step method to incompressible navier-stokes equations. *Journal of Computational Physics* **59** (2), 308–323.

Le Grand, N., Daerr, A. & Limat, L. 2005 Shape and motion of drops sliding down an inclined plane. *J. Fluid Mech.* **541**, 293–315.

McGuan, R., Alizadeh-Birjandi, E., Yan, P., Davis, S. H. & Pirouz Kavehpour, H. 2024 Experimental and theoretical investigation of impinging droplet solidification at moderate impact velocities. *J. Eng. Math.* **148** (1), 6.

Mohammad Karim, A. 2022 A review of physics of moving contact line dynamics models and its applications in interfacial science. *J. Appl. Phys.* **132**, 080701.

Rossinelli, D., Trabacchin, T., Voci, A., Brown, L., Collis, H., Khanwale, M., Zahtila, T., Brouzet, D. & Iaccarino, G. 2025 Crafting software in HPC: a quantitative approach. *Annual Research Briefs,* Center for Turbulence Research, Stanford University, pp. 363-380 .

Voinov, O. V. 1976 Hydrodynamics of wetting. *Fluid Dyn.* **11**, 714–721.

Yan, P. & Kavehpour, P. 2024 Private email communication .

Yue, P. 2020 Thermodynamically consistent phase-field modelling of contact angle hysteresis. *J. Fluid Mech.* **899**, A15.